ACS APPLIED MATERIALS & INTERFACES

www.acsami.org

Research Article

Thermally Activated Processes for Ferromagnet Intercalation in Graphene-Heavy Metal Interfaces

Fernando Ajejas, Alberto Anadon, Adrian Gudin, José Manuel Diez, Cosme G. Ayani, Pablo Olleros-Rodríguez, Leticia de Melo Costa, Cristina Navío, Alejandro Gutierrez, Fabian Calleja, Amadeo L. Vázquez de Parga, Rodolfo Miranda, Julio Camarero, and Paolo Perna*

Cite This: *ACS Appl. Mater. Interfaces* 2020, 12, 4088−4096

Read Online

ACCESS | Metrics & More | Article Recommendations | Supporting Information

ABSTRACT: The development of graphene (Gr) spintronics requires the ability to engineer epitaxial Gr heterostructures with interfaces of high quality, in which the intrinsic properties of Gr are modified through proximity with a ferromagnet to allow for efficient room temperature spin manipulation or the stabilization of new magnetic textures. These heterostructures can be prepared in a controlled way by intercalation through graphene of different metals. Using photoelectron spectroscopy (XPS) and scanning tunneling microscopy (STM), we achieve a nanoscale control of thermally activated intercalation of a homogeneous ferromagnetic (FM) layer underneath epitaxial Gr grown onto (111)-oriented heavy metal (HM) buffers deposited, in turn, onto insulating oxide surfaces. XPS and STM demonstrate that Co atoms evaporated on top of Gr arrange in 3D clusters and, upon thermal annealing, penetrate through and diffuse below Gr in a 2D fashion. The complete intercalation of the metal occurs at specific temperatures, depending on the type of metallic buffer. The activation energy and the optimum temperature for the intercalation processes are determined. We describe a reliable method to fabricate and characterize in situ high-quality Gr-FM/HM heterostructures, enabling the realization of novel spin-orbitronic devices that exploit the extraordinary properties of Gr.

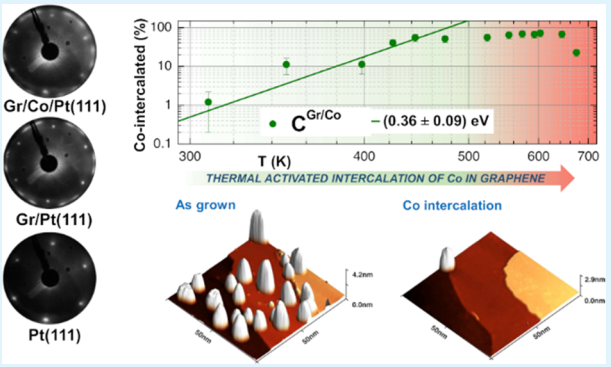

KEYWORDS: *graphene, spin-orbit coupling, surface science, photoemission spectroscopy, scanning tunnel microscopy, epitaxy, oxides*

INTRODUCTION

The future sensing and data storage technologies will be based on the exploitation of the spin-orbit physics in ferromagnetic-heavy metal systems. Graphene (Gr) is considered an ideal material for room temperature (RT) spintronics because of its unique and intrinsically tunable electronic properties.[1−3] However, its technological development for this purpose relies on the capability to engineer high-quality interfaces in which the negligible intrinsic spin-orbit interaction in Gr would be modified to allow for efficient RT spin injection, detection, manipulation, or gating.

The electronic properties of Gr can be tuned by proximity with heavier metallic atoms in hybrid Gr/ferromagnet (FM)[4] or Gr/heavy metal (HM)[5,6] structures. This may enable manipulating (through spin-orbit effects) the electron's spins for information storage and sensing applications more efficiently, faster, and with lower energy consumption than today's commercialized electronics. In particular, when Gr is coupled with a FM, a variety of fundamental and technologically relevant effects have been found, such as high spin injection efficiency,[7] antiferromagnetic coupling,[8] the Rashba effect,[5,9] spin filtering,[10] tunnel magnetoresistance,[11] or enhancement of the magnetic moment perpendicular to the surface.[12−14] More recently, it has been demonstrated that Gr/FM structures allow for RT stable chiral spin textures[13,15] and preserve spins over large distances and long time periods.[16]

A convenient method of fabrication of complex Gr/FM/HM heterostructures is by intercalation, that is, by penetration of ferromagnetic atoms through the Gr sheet, which, acting as a surfactant,[17] will promote an ordered, layer-by-layer, growth below, that is, at the interface between Gr and the initial substrate. This phenomenon has been observed for graphene in a large number of systems, comprising different substrates and a variety of atomic and molecular species.[18] Additionally, Gr protects the intercalated species from air, preventing the oxidation of FM layers in complex spintronic devices.[13,19] There have been several studies to try to identify the mechanisms of intercalation.[18−26] However, to date, there

Received: October 23, 2019
Accepted: December 25, 2019
Published: December 25, 2019

https://dx.doi.org/10.1021/acsami.9b19159
ACS Appl. Mater. Interfaces 2020, 12, 4088−4096

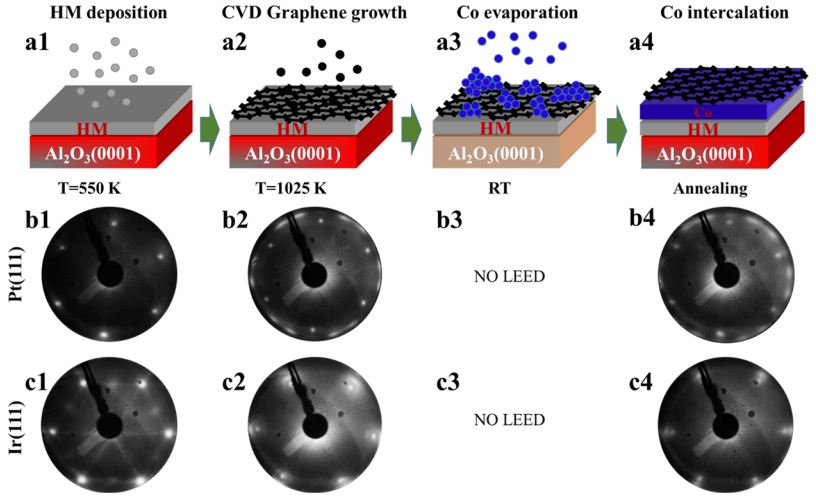

Figure 1. Sketches of the fabrication of the Gr-based heterostructure and corresponding LEED patterns. Schematic of the UHV epitaxial growth process: (a1) dc sputtering deposition of the HM buffer layer (Pt and Ir) at high temperature, (a2) Gr growth by CVD, (a3) e-beam evaporation of five MLs of Co at RT on the Gr surface, and (a4) Co intercalation underneath Gr by thermal annealing. The corresponding LEED patterns (i.e., at each stage of the growth) on the Pt and Ir (111) fcc buffers are shown in panels (b) and (c), respectively. In b2 (b4), the hexagonal diffraction spots correspond to the lattice of Pt (Co, pseudomorphic with Pt). The rings around the spots are due the rotational domains of Gr (oriented at ±15°). In c2 (c4), the spots correspond to the hexagonal fcc lattice of Ir (Co, pseudomorphic with Ir). The circles around the spots are the moiré superstructure of Gr. Note that, in the case of Co on top of Gr (panels a3 to c3), the lack of long-range structural order due to isolated Co clusters is responsible for the absence of the diffraction peaks.

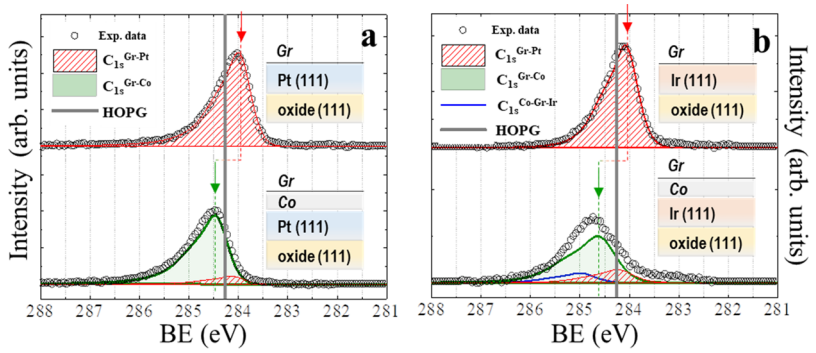

Figure 2. Analysis of the C 1s XPS core levels for Gr/HM and Gr/Co/HM systems. (a, top graph): the C 1s peak appears at binding energy (BE) = 284.0 eV (red component in the fit) in Gr/Pt(111). (a, bottom graph): after the Co intercalation [i.e., Gr/Co/Pt(111)], the C 1s peak is centered at a higher energy (284.5 eV) by +0.5 eV. (b, top graph): the C 1s peak appears at binding energy (BE) = 284.2 eV (red component in the fit) in Gr/Ir(111). (b, bottom graph): after the Co intercalation [i.e., Gr/Co/Ir(111)], the C 1s peak is centered at a higher energy (284.7 eV) by +0.5 eV. The vertical gray line indicates the C 1s peak position corresponding to graphite (HOPG). In both cases, five MLs of Co were evaporated at RT and completely intercalated by thermal annealing. The sketches of the corresponding structures are indicated at the right of the spectra.

are almost no systematic studies that characterize the activation energies involved in the intercalation processes.

In this work, we present a complete study of the growth process of epitaxial Gr-based heterostructures, in which a ferromagnetic Co layer is intercalated between Gr and heavy metallic buffer (Pt and Ir) deposited epitaxially on top of insulating Al_2O_3 (0001) substrates. The structural, chemical, and electronic properties of the surfaces are investigated in situ by surface-sensitive techniques, such as low energy electron diffraction (LEED) and X-ray photoemission spectroscopy (XPS) at each stage of the growth. A close view of the morphology of the surfaces obtained by scanning tunneling microscopy (STM) reveals the specific intercalation processes for cobalt. The first, which is characterized by low activation temperature and relatively low energy barrier, accounts for the penetration of the FM species through Gr. At intermediate temperatures, the Co adatoms diffuse underneath Gr and form a flat, homogeneous layer that continues to grow layer by layer. Higher temperatures finally promote the intermixing of Co with the metallic buffer, which should be avoided since it is, a priori, detrimental for the overall interface properties.

RESULTS AND DISCUSSION

Growth of Gr/Co on Epitaxial HM Buffers onto the (111)-Oriented Insulating Oxide Surface. The samples were prepared entirely in ultrahigh vacuum (UHV) conditions by adopting a specific methodology[13] monitored by in situ surface analysis, as schematically shown in Figure 1: first (panel a1), 30 nm-thick, epitaxial, single-crystal, Pt(111) or Ir(111) buffers were grown by dc sputtering at 550 K on commercial Al_2O_3(0001) single-crystal substrates. The HM buffers present a crystal quality equivalent to Pt(111) and Ir(111) single crystals, as judged from the corresponding LEED patterns (Figure 1, b1 and c1). Second (panel a2), epitaxial layers of graphene were grown in situ by ethylene chemical vapor deposition at 1025 K on top of the buffers. In the case of the

https://dx.doi.org/10.1021/acsami.9b19159
ACS Appl. Mater. Interfaces 2020, 12, 4088−4096

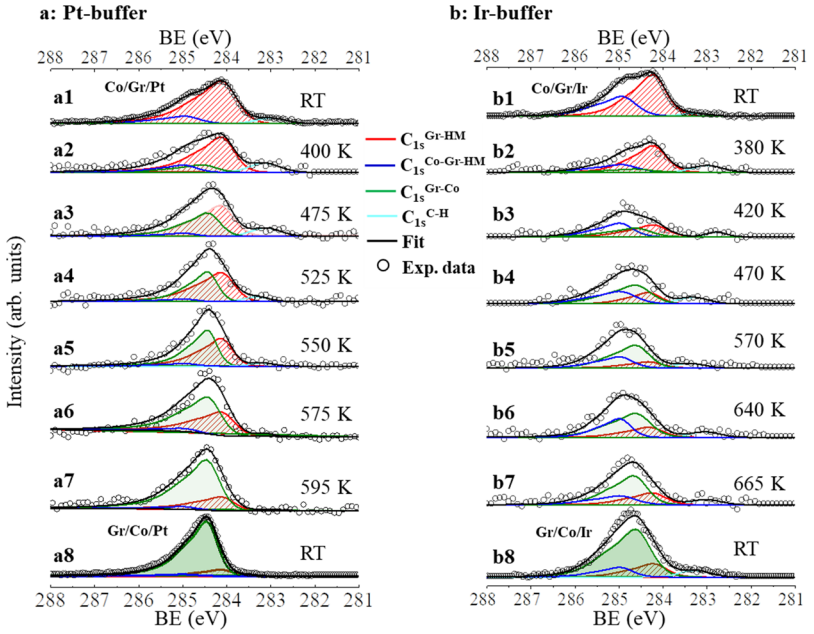

Figure 3. Temperature evolution of the C 1s XPS spectra. XPS of the C 1s region for five MLs of Co annealed at different temperatures. (a1−a8) C 1s spectra for Gr/Pt(111) from RT up to 595 K. (b1−b8) C 1s spectra of Gr/Ir(111) from RT up to 665 K. The spectra in (a8) and (b8) were acquired after cooling the sample back to RT. The additional component at 283.2 eV was introduced to account for leftovers of ethylene dissociation. Black lines are the fitting curves including all the components. See the main text for a detailed description.

Pt(111) buffer, the typical LEED rings (Figure 1, b2) are due to the characteristic[27,28] multidomain Gr flakes, that is, domains oriented at ±15°. The different domains are also revealed by STM on the as-grown samples (see Figure S2). On the contrary, Gr grown on the Ir(111) buffers presents a LEED pattern (Figure 1, c2), corresponding to the well-known "10 × 10" moiré pattern due to the incommensurate unit cells of Ir and Gr.[29]

Third (panel a3), five monolayers (MLs) of thick cobalt films were evaporated on top of graphene by molecular beam epitaxy (MBE) at RT with a low deposition rate of 0.3 Å/s monitored by an in situ quartz balance. Finally (panel a4), the temperature was raised to activate the intercalation processes studied by surface microscopy and spectroscopies. After the intercalation process, the LEED patterns of the initial Gr/Pt(111) of Gr/Ir(111) surfaces are recovered (Figure 1, b4 and c4, respectively). This indicates that the intercalated Co is pseudomorphic with the metallic substrates, epitaxial and (111)-oriented, as well as homogeneously (over $\sim\mu m^2$) intercalated underneath Gr. Thus, by following this growth methodology, homogeneous epitaxial face-centered cubic (fcc) cobalt layers sandwiched between the HM buffers and Gr were obtained.[13]

Figure 2 shows the XPS spectra of the C 1s core levels of Gr grown on Pt (panels a) and Ir (panels b) buffers before the evaporation of Co and after its intercalation. The C 1s XPS signals in both structures are clearly visible after the growth of Gr on top of the epitaxial buffers (top panels). The C 1s line shape is fitted with one main asymmetric component corresponding to the bonds of C atoms of graphene with each HM. In the case of the Pt buffer (panel a), the C 1s peak is found at binding energy (BE) = 284.0 eV (C^{Gr-Pt}, red patterned area), whereas for the Ir buffer (panel b), the C 1s peak is at BE = 284.2 eV (C^{Gr-Ir}, red patterned area). The energy position of peaks reflect the sp^2 hybridization of C−C bonding for Gr on weakly interacting Pt(111) and Ir(111) substrates.[30] The C 1s level in Gr/Pt(111) [Gr/Ir(111)] is shifted to a lower binding energy (BE) by −0.3 eV [−0.1 eV] with respect to the one of HOPG[27,31] (vertical gray line in panels a and b), reflecting the doping of Gr on these substrates.[30,32,33]

After RT evaporation of five MLs of Co and thermal annealing during 30 min at 595 K for Pt and at 665 K for the Ir buffer, Co is completely intercalated underneath the Gr sheet. The XPS spectrum in the bottom panel of Figure 2a shows, for the Pt buffer, a C 1s peak centered at BE = 284.5 eV (i.e., C^{Gr-Co}, filled green area), that is, shifted by +0.5 eV toward higher BE than the original C^{Gr-Pt}. The C 1s peak in the Ir buffer structure (bottom panel in Figure 1b) is centered at BE = 284.7 eV (i.e., C^{Gr-Co}, filled green area), that is, shifted by +0.5 eV toward higher BE than the original C^{Gr-Ir}. Thus, the insertion of Co results in a Gr surface with opposite doping with respect to the Gr/Pt and Gr/Ir structures.

These results are consistent with the predicted values of the BEs of the C 1s core level of graphene on various metals,[32] which depends essentially on the respective metal work functions, being Gr p-doped on Pt and Ir and n-doped on Co. The observed shifts in both structures account for the presence of an electric field gradient at the Gr/Co top interface that gives rise to a Rashba-type Dzyaloshinskii−Moriya interaction (DMI) as argued in a previous work.[13] A similar band shift, with Rashba character, was also experimentally found in Gr/Au[5] and Gr/Pb.[34,35]

Co Intercalation in Gr/HM Buffer. To have a detailed picture of the Co intercalation processes, we have acquired fast (∼1 min long) XPS spectra of the C 1s peaks during in situ thermal annealing from RT up to ∼680 K. The temperature was raised with a rate of ∼1 K/min by means of a radiative heater placed under the sample.

Representative C 1s spectra as function of the temperature are shown in Figure 3a after Co evaporation on the Pt buffer. The scans in panels (a1) and (a8) were performed at RT with

https://dx.doi.org/10.1021/acsami.9b19159
ACS Appl. Mater. Interfaces 2020, 12, 4088−4096

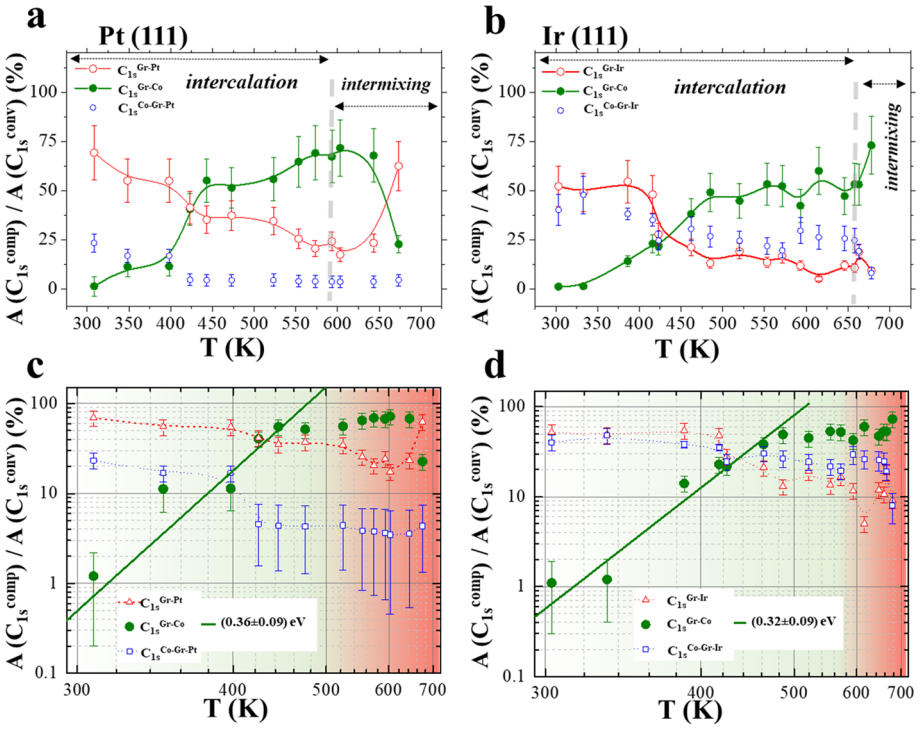

Figure 4. Monitoring of Co intercalation in Gr/Pt and Gr/Ir. (a, b) Temperature evolution of area percentage of the $C^{Gr\text{-}Co}$ (green symbols), $C^{Co\text{-}Gr\text{-}HM}$ (blue), and $C^{Gr\text{-}HM}$ (red) components (A^{comp}_{C1s}) normalized by the total area of the C 1s peak (A^{conv}_{C1s}), as taken by the XPS spectra. Two temperature ranges, indicated by gray vertical lines, are identified. In the low-temperature regions, that is, from 300 to 595 K for Pt and from 300 to 645 K for Ir, Co atoms penetrate and then diffuse underneath Gr, respectively. Above 600 K (for Pt buffer in panel a) and 645 K (for Ir, panel b), the increase of $C^{Gr\text{-}HM}$ and decrease of $C^{Gr\text{-}Co}$ correspond to a scenario in which Co atoms diffuse into the HM layer, while HM atoms move toward the surface. Panels (c) and (d) present in Log scale the ratio $A = A^{comp}_{C1s}/A^{conv}_{C1s}$ as a function of T in the reciprocal scale. The linear fits (green continuous lines) of $C^{Gr/Co}$ component give the activation energies of the intercalation process.

better statistics and correspond to initial stage of Co/Gr/Pt(111) and to the final, fully intercalated Gr/Co/Pt(111) case, respectively, as reproduced in Figure 2.

At each temperature, the C 1s spectrum is fitted with three components: $C^{Gr\text{-}Pt}$ (red patterned area) centered at BE = 284.0 eV that corresponds to the Gr bonding to Pt(111) (unperturbed sp^2 atoms);[30] $C^{Co\text{-}Gr\text{-}Pt}$ (blue) at 285.0 eV that corresponds to C atoms sandwiched between Co and Pt, that is, those below the Co islands grown on Gr/Pt(111) (probably due the trapping of the metal atoms into Gr defects);[26] and $C^{Gr\text{-}Co}$ (green) at 284.5 eV due to the C atoms interacting exclusively with the intercalated Co as confirmed by the intensity increase during the annealing. An additional C 1s component at 283.2 eV, which disappears upon annealing, was introduced to account for leftovers of ethylene dissociation.[21,36]

If the evaporation of Co would produce a flat Co film covering homogeneously the Gr/Pt(111) substrate prior to the annealing procedure, then the area of the $C^{Co\text{-}Gr\text{-}Pt}$ (blue) component in panel (a1) should be dominant. Instead, we found that the former (component at 285.0 eV) is only 25% of the total area. This indicates that, right after evaporation, only a relatively small fraction of the area investigated by XPS ($\sim\mu m^2$) is covered by Co, while most of the surface is not covered. This suggests a disordered or Volmer−Weber growth mode of Co on top of Gr at RT. In fact, the formation of disordered clusters is consistent with the absence of LEED patterns in Figure 1. This is further confirmed by STM experiments shown below in Figures 5 and 6.

At 400 K (panel a2), the C 1s component at BE = 284.5 eV due to the C atoms placed on top of Co atoms, that is, $C^{Gr\text{-}Co}$ (green filled area), increases to 13%, indicating a noticeable intercalation, while the $C^{Co\text{-}Gr\text{-}Pt}$ (blue) component is slightly reduced to about 15% of the total. This indicates that the intercalation occurs at the expense of the area covered by Co clusters. At 475 K (panel a3), the $C^{Co\text{-}Gr\text{-}Pt}$ component is drastically reduced with a substantial increase in the green intercalated component, which indicates that the Co clusters are disappearing and almost all Co atoms are intercalated. Nevertheless, the $C^{Gr\text{-}Pt}$ (red) component is still >40% of the total area, meaning that a significant fraction of the initial Gr/Pt surface is not yet intercalated. From 525 K (panel a4) on the $C^{Gr\text{-}Pt}$ component starts to decrease, while the $C^{Gr\text{-}Co}$ slowly increases (panels a5−a7). At 595 K (panel a7), the former is almost totally suppressed, while the latter becomes maximum. The formation of this flat, 2D intercalated Co layer is confirmed by the fact that the LEED pattern observed in Gr/Pt(111) is recovered. By analyzing the fraction of the area of each component with respect to the total, we found that more than 75% of the total area of the C 1s peak corresponds to intercalated Co, that is, Gr with Co underneath, while the other two components, indicating that C atoms are still in contact with the Pt layer (~20%, nonintercalated area) and with Co on the top (<5%, remaining clusters), are strongly reduced. This quantifies the completeness and uniformity of the intercalation process. Thus, upon intercalation at 595 K, the Co atoms spread underneath Gr to form pseudomorphic MLs in a step flow-like mode.[24]

https://dx.doi.org/10.1021/acsami.9b19159
ACS Appl. Mater. Interfaces 2020, 12, 4088−4096

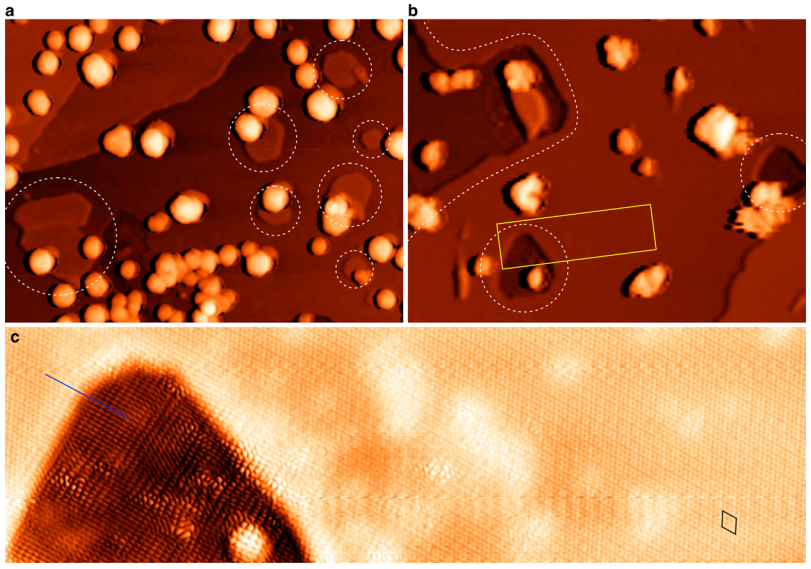

Figure 5. Initial stages of intercalation. Panels (a) and (b) show 100 nm wide STM images recorded at +1 V bias and 200 pA tunneling current on the (a) early and (b) final stages of the intercalation of the first ML of Co at 500 and 900 K. Interface regions between the nonintercalated graphene and the first Co interlayer are highlighted in white dash. Panel (c) presents a 35 nm wide STM image with atomic resolution recorded at +30 mV bias and 3 nA tunneling current on the area marked by the yellow rectangle on panel (b). The black rhombus highlights a 4 × 4 moiré pattern in the intercalated region, and the blue line marks a high symmetry direction of the graphene lattice across the interface between the intercalated and nonintercalated regions.

The most representative C 1s spectra as function of the temperature after the Co evaporation in the Ir buffer are shown in Figure 3b. The scans in panels (b1) and (b8) were performed at RT with more statistics and correspond to the initial (i.e., Co/Gr/Ir) and final (Gr/Co/Ir) stages of the intercalation process, respectively.

As described above, the C 1s spectra are fitted at each temperature using three components: $C^{Gr\text{-}Ir}$ (red patterned area) at BE = 284.2 eV (in agreement with refs 31 30, and 33); $C^{Gr\text{-}Co}$ (green) at 284.7 eV due to the C atoms interacting exclusively with the intercalated Co; and $C^{Co\text{-}Gr\text{-}Ir}$ (blue) at 285.0 eV that corresponds to C atoms sandwiched between Co and Ir. The component at 283.2 eV was introduced to account for leftovers of ethylene dissociation.[31,36]

After the Co evaporation and prior to annealing (panel b1), a large $C^{Co\text{-}Gr\text{-}Ir}$ (blue) component is found, unlike the case of the Pt buffer. This suggests that a coverage of the graphene surface by Co clusters is larger than in the case of Gr/Pt(111). At 420 K (panel b3), the increase in the intensity of the C 1s $C^{Gr\text{-}Co}$ component (green) at BE = 284.7 eV indicates a substantial intercalation. By increasing the temperature below 600 K (panels b4 and b5), the area of this component increases, indicating the formation of a continuous Co layer below Gr, while $C^{Gr\text{-}Ir}$ decreases to less than 17% of the total. This behavior is analogous to the case of the Pt buffer. By analyzing the fraction of the area of each component with respect to the total, we found that ∼60% of the total area of the C 1s peak corresponds to intercalated Co. If the temperature is further increased (panels b6 and b7), we notice the slight increase of the $C^{Gr\text{-}Ir}$ (red line), evidencing the intermixing of intercalated Co into the Ir buffer.

XPS spectra at each stage of growth in the region of the Pt 4d, Ir 4d, and Co 2p core levels for Pt and Ir buffers are shown in Figure S1. Note that the analyses of the area and position of the Pt and Ir 4d core levels as well as the Co 2p levels during the intercalation processes indicates the absence of Co/HM intermixing at temperatures below 650 K.

Thermally Activated Mechanisms for Co Intercalation. The intercalation processes of different atomic species through epitaxial Gr have been interpreted in terms of diffusion of atoms through Gr island edges,[18] wrinkles and defects,[22] or direct exchange with carbon atoms.[18,20] The energy required to activate each of these mechanisms is experimentally delivered by thermal annealing and depends on the specific substrate onto which the Gr is grown and on the atomic species to be intercalated. DFT calculations indicate that the presence of a substrate lowers the energy barrier for the intercalation compared to free standing Gr and that adatoms on top of Gr further reduce such a barrier.[23,37]

In weakly interacting metallic substrates, such as Gr/Ir(111), Decker et al.[14] found that the intercalation proceeds mainly via migration of atoms through Gr patch edges. Instead, the superior surface quality of highly interacting Gr/Ru(0001) interfaces,[36,38] with few preexisting defects, makes energetically less favored the penetration through edges or wrinkles,[20] while the cooperative effect of the presence of the substrate and Co clusters favors the formation of surface defects enabling, hence the direct penetration through the Gr sheet.[37]

Figure 4 shows the area of each component in the C 1s XPS spectra (A_{C1s}^{comp}) as function of the temperature. These areas (divided by the total area, A_{C1s}^{conv}) account for the amount of Co atoms in the different structures. In Figure 4, we can distinguish two temperature regions. The first, from RT to 595 and 645 K for Pt and Ir, respectively, corresponds to the Co intercalation, while the high-temperature region corresponds to the Co/HM intermixing.

In the case of the Pt buffer (panel a), the first region, from RT to 445 K, is characterized by an exponential increase of the $C^{Gr\text{-}Co}$ component area (green symbols) and by a reduction of the $C^{Gr\text{-}Pt}$ (red). Both components do not substantially change from 475 up to 595 K, displaying an almost saturated behavior.

https://dx.doi.org/10.1021/acsami.9b19159
ACS Appl. Mater. Interfaces 2020, 12, 4088−4096

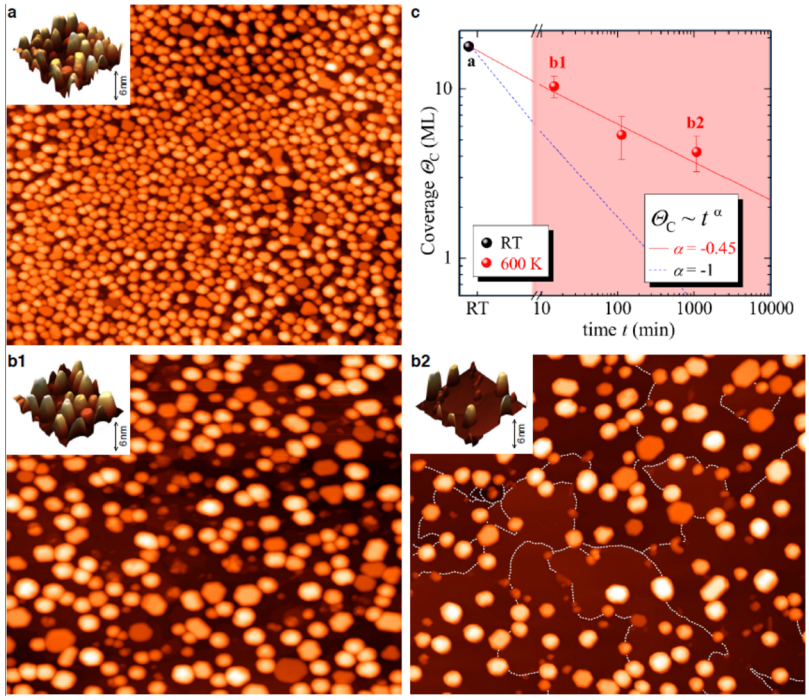

Figure 6. Intercalation dynamics of 18ML Co studied by STM. Side STM images (250 nm) recorded at +1 V bias and 200 pA tunneling current on the (a) nonannealed surface, annealed to 600 K for 10 min (panel b1) and kept at 600 K for 1000 min (panel b2). The corresponding insets show 50 nm wide cuts represented in 3D. In panel (b2), the monoatomic steps in between Co clusters have been highlighted with white dashed lines. All images have been recorded at RT. (c) Time evolution of the effective coverage of Co clusters, obtained from the volume analysis of the complete STM annealing sequence (see Figure S3).

The $C^{Gr\text{-}Co}$ reaches about 75% of the total area, while the $C^{Gr\text{-}Pt}$ drops to less than 20% and the $C^{Co\text{-}Gr\text{-}Pt}$ reduces to <5% at 600 K. Finally, the annealing above 650 K causes the increase of the $C^{Gr\text{-}Pt}$ and the simultaneous drop of the $C^{Gr\text{-}Co}$, indicating that Pt atoms move toward the surface while Co atoms diffuse into the Pt layer (intermixing).

To determine the average activation energy (E_a) of the intercalation process, we have assumed that $A = A_{C1s}^{comp}/A_{C1s}^{conv}$ can be written as $A(T) \propto e^{-E_a/k_BT}$, where k_B is the Boltzmann constant. From the corresponding plot as a function of $1/k_BT$ shown in Figure 4c, an activation energy for the process of Co intercalation underneath Gr/Pt(111) of E_a (Pt) = 0.36 ± 0.09 eV can be obtained.

A similar behavior is also found in the case of Ir buffer (panel b). However, we can appreciate easily some differences. First, in Gr/Ir(111), about 50% of the evaporated sample area is initially covered by Co clusters; second, the intercalation requires a slightly higher temperature than in Gr/Pt; and third, at the end of the process, only 60% of the evaporated Co has been intercalated. The process requires an activation energy comparable to the one found in the Pt case, that is, E_a (Ir) = 0.32 ± 0.09 eV. These results evidence a somewhat less efficient intercalation mechanism through the Gr/Ir surface than on Gr/Pt in agreement with the larger interaction between Gr and Ir[29] compared to Pt[27,28] and the lack of domain edges indicated by the LEED pattern of Gr/Ir(111) and Gr/Co/Ir(111), which shows a moiré pattern without rotational domains. Notice that the intermixing and alloying between Co and Ir, as indicated by the increase of the $C^{Gr\text{-}Ir}$ component, is detected around 650 K, while the intercalation of Co atoms is still proceeding ($C^{Gr\text{-}Co}$ increases).

To confirm the above picture, an additional STM study was conducted under UHV and in similar conditions to the XPS study for the case of the Pt(111) buffer. First, the Co-free surface of Gr/Pt/oxide(111) revealed atomically flat and large Gr flakes with a large variety of rotational domains, as shown in Figure S2, and in agreement with the LEED characterizations discussed above (Figure 1). Then, different amounts of Co were evaporated at RT, and the sample was annealed at various temperatures while checking the surface evolution by means of STM imaging at RT (Figure 5).

We first studied the initial stages of intercalation by preparing a low coverage sample, with a nominal Co coverage of two MLs. Upon evaporation at RT, Co forms 3D clusters covering only a small fraction of the Gr surface, as deduced above from the XPS results. Annealing the sample to 500 K for 10 min results in the STM image shown in Figure 5a. Some intercalated regions are indicated by the white dashed circles showing that, in the initial stages, Co penetrates through Gr below the clusters, suggesting a direct Co-C exchange mechanism. Further annealing to 900 K resulted in the completion of the first Co interlayer, as illustrated in Figure 5b.

As further proof of the intercalation, an atomic resolution STM image corresponding to the region highlighted in yellow in Figure 5b is presented in panel (c). The atomic lattice of Gr is continuously resolved both in the intercalated (right) and in the nonintercalated (left) areas, along by the blue line. Also note that a quasi-4 × 4 moiré pattern, arising from the mismatch between graphene and the underlying surface, is clearly detected in the intercalated area (unit cell marked in black in the lower right corner). This pattern is not resolved in the nonintercalated area due to the presence of a strong intervalley scattering signal. Note that the temperature for

https://dx.doi.org/10.1021/acsami.9b19159
ACS Appl. Mater. Interfaces 2020, 12, 4088−4096

intercalation at low Co coverages is higher compared to the larger coverages discussed previously and in the following.

Figure 6 shows the time evolution at a constant annealing temperature of 600 K of an initial Co coverage of 18 MLs. In this case, similar deposition rates for Co and annealing temperatures to the XPS study were used. The as-deposited surface (panel a) presents a large array of Co clusters, with an average height of 4.7 nm and an average radius of 5.0 nm, in agreement with the 3D growth of Co on Gr at RT, as previously discussed. As the sample is annealed, the cluster density decreases, exposing gradually the intercalated Gr surface (panels b1 and b2). Note that we did not observed any evidence of expansion of the clusters on the Gr surface, suggesting an out-of-plane diffusion of Co atoms. The total Co cluster effective coverage Θ_C, obtained from the cluster volume in the STM images, is shown in panel (d) for the complete annealing sequence. The cluster coverage evolves from 18 MLs, that is, before any annealing, to near 10 MLs after 10 min 600 K annealing (panel b1), decreasing to 4 MLs after the last annealing (1000 min, panel b2). The presence of monoatomic steps in between the remaining Co clusters in the annealed surface (best resolved in panel c, where they are highlighted in white dash) is a clear indication of an in-plane diffusion of the intercalated species underneath the surface (2D process), in agreement with the previous analysis of the XPS data. This is also evinced by the analysis of the submonolayer regime discussed in Figure S4. The worm-like structures highlighted in the yellow box in Figure S4b, in fact, are the precursors of the 2D Co intercalated layer that occurs at higher coverages. As a proof that the worm-like structures are intercalated underneath graphene, Figure S4c presents an atomic resolution STM image of them, where the graphene atomic lattice can be resolved continuously all over the surface.

Panel (c) provides additional qualitative insights onto the dynamics of the intercalation processes. For instance, the clusters' effective coverage displays an inverse law evolution with the square root of the annealing time, that is, the intercalated Co thickness varies as the square root of the time (t), as expected for a universal random walk (Brownian motion) diffusion (out-of-plane) process: $\Theta_C \propto t^{\alpha}$, with α is approximately -0.45 ± 0.05.

In summary, the combined study of XPS and STM reveals that (i) Co atoms evaporated on top of Gr agglomerate to form 3D clusters, and (ii) the intercalation is activated thermally at a specific temperature. Upon thermal annealing, Co atoms penetrate directly through Gr below the clusters. Subsequently, Co starts to diffuse underneath Gr and form a homogeneous layer. For a much higher temperature, Co and HM atoms intermix. The first two processes define the complete intercalation of the metal underneath Gr and follow a behavior that can be characterized by an activation energy of the order of 0.3 eV, as clearly identified in Figure 4a.

One should note that an incomplete Co intercalation leads to a depressed interface and magnetic properties due to (i) the oxidation of the FM not protected by Gr, (ii) undefined electronic band gap of Gr, and (iii) negligible effective interfacial DMI. Our in situ analysis allows controlling the surface properties of each layer and avoiding incomplete intercalation and alloy formation, which are mainly caused by under and over thermal annealing, respectively.

CONCLUSIONS

In this work, we have introduced a novel methodology based on the combined use of ultrahigh vacuum growth, metal intercalation, spectroscopy, and tunneling microscopy to fabricate and characterize in situ high-quality Gr-based, perpendicular magnetic anisotropy systems. By combining XPS and STM experiments as functions of the annealing temperature, we have discerned the processes of Co intercalation underneath Gr grown epitaxially on two different heavy metal surfaces, Pt and Ir, which were deposited onto (111)-oriented insulating oxides. The thermally activated Co intercalation occurs in two steps in which the deposited atoms penetrate in Gr either via direct Co-C exchange or through surface defects and edges. The intercalated atoms diffuse then in 2D underneath Gr and form flat, homogeneous, and crystalline layers. These processes are characterized by a low activation temperature. The Co intercalation occurs at lower temperature and is more efficient in Gr/Pt interfaces than Gr/Ir. Higher temperatures promote the intermixing between the FM and the metallic buffer. We have hence demonstrated that the metal intercalation allows for efficient tuning of the structural and electronic properties of Gr and enables the growth of high-quality flat layers with tailored magnetic properties.

METHODS

Growth. The substrates used in the experiments were 10 mm-thick, 5 × 5 mm^2 prepolished Al_2O_3 (0001) single crystals. Figure 1 shows the scheme of the growth process. The substrate was placed in a vacuum chamber with a base pressure of $\sim 10^{-8}$ mbar and annealed at 700 K during 1 h prior to the deposition. The epitaxial growth of the buffer layer (panel a1 in Figure 1) was performed by dc sputtering Ar^+ deposition with a partial gas pressure of 10^{-3} mbar at 15 W magnetron power, with parallel configuration between the sample and target whose distance was set to 5 cm. The deposition rate was measured by in situ quartz balance. After the deposition, the sample was cooled down to RT. Two different buffer HM layers [Pt(111) and Ir(111)] have been grown. In situ LEED measurements confirm the epitaxial growth of both buffers and the fcc structure (ABC stacking sequence). Gr was then grown in situ by ethylene (C_2H_4) dissociation (partial pressure of 2×10^{-8} mbar during 30 min) at 1025 K during 1 h in UHV (base pressure of 10^{-9} mbar). The sample was then cooled to RT, and the FM layer was evaporated by molecular beam epitaxy (MBE) at 0.04 Å/s. The sample was gradually heated up while acquiring XPS spectra for the real-time study of the intercalation process.

Photoemission Experiments. At each stage of the growth process, we have performed careful LEED and XPS measurements. The XPS measurements were performed by using a monochromatized X-ray source and a hemispherical energy analyzer (SPHERA-U7). The Al Kα line ($h\nu$ = 1486.7 eV) was used from an Al anode for X-ray photoelectron spectroscopy (XPS). The analyzer pass energy was set to 20 eV for the XPS measurements to have a resolution of 0.6 eV. The angular acceptance for the used aperture size is defined solely by the magnification mode, that is, 1750 × 2750 μm^2. The core level spectra were fitted to mixed Gaussian−Lorentzian components; all the binding energies are referred to the sample Fermi level. In the fits presented in Figure 3, an additional component centered at 283.2 eV was introduced, accounting for leftovers of ethylene dissociation (C^{C-H}). This component was only needed in the first low-temperature spectra of the thermal annealing.

Scanning Tunneling Microscopy. STM measurements have been performed in an independent UHV chamber equipped with an Omicron variable temperature STM (VT-STM 25). The STM head was operated with a Nanonis electronics. Bias voltages given in the manuscript refer to the sample voltage. Gr/Pt/oxide samples were

https://dx.doi.org/10.1021/acsami.9b19159
ACS Appl. Mater. Interfaces 2020, 12, 4088−4096

prepared ex situ, as explained in the Growth section, transported to the STM chamber in air and subsequently annealed in situ to remove air contamination. Co evaporation and the annealing sequences leading to the intercalation process were performed in situ, as explained in the main text. The effective Co coverage was obtained from the STM images by multiplying the average cluster height by the fraction of the total area occupied by the clusters. All STM measurements have been performed at room temperature.

■ ASSOCIATED CONTENT

Supporting Information

The Supporting Information is available free of charge at https://pubs.acs.org/doi/10.1021/acsami.9b19159.

X-ray photoemission spectroscopy (XPS) at Pt, Ir 4d, and Co 2p edges (Figure S1), scanning tunneling microscopy (STM) analysis of the Gr/Pt/Al_2O_3(0001) surface (Figure S2), Co cluster coverage evolution monitored by STM (Figure S3), and submonolayer regime studied by STM (Figure S4) (PDF)

■ AUTHOR INFORMATION

Corresponding Author

Paolo Perna − *IMDEA Nanociencia, Madrid, Spain;* orcid.org/0000-0001-8537-4834; Email: paolo.perna@imdea.org

Other Authors

Fernando Ajejas − *IMDEA Nanociencia, Madrid, Spain, and Universidad Autónoma de Madrid, Madrid, Spain*

Alberto Anadon − *IMDEA Nanociencia, Madrid, Spain*

Adrian Gudin − *IMDEA Nanociencia, Madrid, Spain, and Universidad Autónoma de Madrid, Madrid, Spain*

José Manuel Diez − *IMDEA Nanociencia, Madrid, Spain, and Universidad Autónoma de Madrid, Madrid, Spain*

Cosme G. Ayani − *IMDEA Nanociencia, Madrid, Spain*

Pablo Olleros-Rodríguez − *IMDEA Nanociencia, Madrid, Spain*

Leticia de Melo Costa − *IMDEA Nanociencia, Madrid, Spain*

Cristina Navío − *IMDEA Nanociencia, Madrid, Spain*

Alejandro Gutierrez − *Universidad Autónoma de Madrid, Madrid, Spain*

Fabian Calleja − *IMDEA Nanociencia, Madrid, Spain;* orcid.org/0000-0001-6007-8641

Amadeo L. Vázquez de Parga − *IMDEA Nanociencia, Madrid, Spain, Universidad Autónoma de Madrid, Madrid, Spain, and IFIMAC, Universidad Autónoma de Madrid, Madrid, Spain;* orcid.org/0000-0003-0551-1603

Rodolfo Miranda − *IMDEA Nanociencia, Madrid, Spain, Universidad Autónoma de Madrid, Madrid, Spain, and IFIMAC, Universidad Autónoma de Madrid, Madrid, Spain*

Julio Camarero − *IMDEA Nanociencia, Madrid, Spain, Universidad Autónoma de Madrid, Madrid, Spain, and IFIMAC, Universidad Autónoma de Madrid, Madrid, Spain*

Complete contact information is available at: https://pubs.acs.org/10.1021/acsami.9b19159

Author Contributions

P.P. conceived and designed the project with assistance from F.A., J.C., and R.M. F.A., A.A., and A.G. contributed equally to this work realizing the growth, XPS-UPS, LEED, and magnetometry experiments with the help of J.M.D., P.O.-R., L.d.M.C., C.N., and A.G. F.C., C.G.A., and A.L.V.d.P. performed the STM experiments. F.A., A.A., F.C., and P.P. treated and analyzed the data. P.P. prepared the manuscript with the help of F.A., A.A., F.C., J.C., and R.M. All authors discussed and commented on the manuscript.

Notes

The authors declare no competing financial interest.

■ ACKNOWLEDGMENTS

This research was supported by the Regional Government of Madrid through projects P2018/NMT-4321 (NANOMAG-COST-CM) and P2018/NMT-4511 (NMAT2D) and by the Spanish Ministry of Economy and Competitiveness (MINECO) through projects RTI2018-097895-B-C42, FIS2016-78591-C3-1-R, PGC2018-098613-B-C21, PGC2018-093291-B-I00, FIS2015-67367-C2-1-P, and PCIN-2015-111 (FLAG-ERA JTC2015 Graphene Flagship "SOgraph"). IFIMAC acknowledges support from the "Maria de Maeztu" programme for units of Excellence in R&D (MDM-2014-0377). IMDEA Nanoscience is supported by the "Severo Ochoa" programme for the Centres of Excellence in R&D, MINECO (grant number SEV-2016-0686).

■ REFERENCES

(1) Castro Neto, A. H.; Guinea, F.; Peres, N. M. R.; Novoselov, K. S.; Geim, A. K. The Electronic Properties of Graphene. *Rev. Mod. Phys.* **2012**, *81*, 109−162.

(2) Han, W.; Kawakami, R. K.; Gmitra, M.; Fabian, J. Graphene Spintronics. *Nat. Nanotechnol.* **2014**, *9*, 794−807.

(3) Roche, S.; Åkerman, J.; Beschoten, B.; Charlier, J.-C.; Chshiev, M.; Dash, S. P.; Dlubak, B.; Fabian, J.; Fert, A.; Guimarães, M.; Guinea, F.; Grigorieva, I.; Schönenberger, C.; Seneor, P.; Stampfer, C.; Valenzuela, S. O.; Waintal, X.; van Wees, B. Graphene Spintronics: The European Flagship Perspective. *2D Mater.* **2015**, *2*, 3.

(4) Varykhalov, A.; Sánchez-Barriga, J.; Shikin, A. M.; Biswas, C.; Vescovo, E.; Rybkin, A.; Marchenko, D.; Rader, O. Electronic and Magnetic Properties of Quasifreestanding Graphene on Ni. *Phys. Rev. Lett.* **2008**, *101*, 1−4.

(5) Marchenko, D.; Varykhalov, A.; Scholz, M. R.; Bihlmayer, G.; Rashba, E. I.; Rybkin, A.; Shikin, A. M.; Rader, O. Giant Rashba Splitting in Graphene due to Hybridization with Gold. *Nat. Commun.* **2012**, *3*, 1232.

(6) Calleja, F.; Ochoa, H.; Garnica, M.; Barja, S.; Navarro, J. J.; Black, A.; Otrokov, M. M.; Chulkov, E. V.; Arnau, A.; Vázquez de Parga, A. L.; Guinea, F.; Miranda, R. Spatial Variation of a Giant Spin−orbit Effect Induces Electron Confinement in Graphene on Pb Islands. *Nat. Phys.* **2014**, *11*, 43−47.

(7) Dlubak, B.; Martin, M.-B.; Deranlot, C.; Servet, B.; Xavier, S.; Mattana, R.; Sprinkle, M.; Berger, C.; De Heer, W. A.; Petroff, F.; Anane, A.; Seneor, P.; Fert, A. Highly Efficient Spin Transport in Epitaxial Graphene on SiC. *Nat. Phys.* **2012**, *8*, 557−561.

(8) Gargiani, P.; Cuadrado, R.; Vasili, H. B.; Pruneda, M.; Valvidares, M. Graphene-based Synthetic Antiferromagnets and Ferrimagnets. *Nat. Commun.* **2017**, *8*, 669.

(9) Dedkov, Y. S.; Fonin, M.; Rüdiger, U.; Laubschat, C. Rashba Effect in the Graphene/Ni(111) System. *Phys. Rev. Lett.* **2008**, *100*, 107602.

(10) Karpan, V. M.; Giovannetti, G.; Khomyakov, P. A.; Talanana, M.; Starikov, A. A.; Zwierzycki, M.; van den Brink, J.; Brocks, G.; Kelly, P. J. Graphite and Graphene as Perfect Spin Filters. *Phys. Rev. Lett.* **2007**, *99*, 176602.

(11) Cobas, E.; Friedman, A. L.; van't Erve, O. M. J.; Robinson, J. T.; Jonker, B. T. Graphene As a Tunnel Barrier: Graphene-Based Magnetic Tunnel Junctions. *Nano Lett.* **2012**, *12*, 3000−3004.
(12) Rougemaille, N.; N'Diaye, A. T.; Coraux, J.; Vo-Van, C.; Fruchart, O.; Schmid, A. K. Perpendicular Magnetic Anisotropy of Cobalt Films Intercalated under Graphene. *Appl. Phys. Lett.* **2012**, *101*, 2012−2015.
(13) Ajejas, F.; Gudín, A.; Guerrero, R.; Anadón Barcelona, A.; Diez, J. M.; de Melo Costa, L.; Olleros, P.; Niño, M. A.; Pizzini, S.; Vogel, J.; Valvidares, M.; Gargiani, P.; Cabero, M.; Varela, M.; Camarero, J.; Miranda, R.; Perna, P. Unraveling Dzyaloshinskii−Moriya Interaction and Chiral Nature of Graphene/Cobalt Interface. *Nano Lett.* **2018**, *18*, 5364−5372.
(14) Decker, R.; Brede, J.; Atodiresei, N.; Caciuc, V.; Blügel, S.; Wiesendanger, R. Atomic-scale Magnetism of Cobalt-intercalated Graphene. *Phys. Rev. B* **2013**, *87*, No. 041403.
(15) Yang, H.; Chen, G.; Cotta, A. A. C.; N'Diaye, A. T.; Nikolaev, S. A.; Soares, E. A.; Macedo, W. A. A.; Liu, K.; Schmid, A. K.; Fert, A.; Chshiev, M. Significant Dzyaloshinskii−Moriya Interaction at Graphene−ferromagnet Interfaces due to the Rashba Effect. *Nat. Mater.* **2018**, *17*, 605−609.
(16) Gebeyehu, Z. M.; Parui, S.; Sierra, J. F.; Timmermans, M.; Esplandiu, M. J.; Brems, S.; Huyghebaert, C.; Garello, K.; Costache, M. V.; Valenzuela, S. O. Spin Communication over 30 μm Long Channels of Chemical Vapor Deposited Graphene on SiO_2. *2D Mater.* **2019**, *6*, No. 034003.
(17) Vlaic, S.; Rougemaille, N.; Artaud, A.; Renard, V.; Huder, L.; Rouvière, J.-L.; Kimouche, A.; Santos, B.; Locatelli, A.; Guisset, V.; David, P.; Chapelier, C.; Magaud, L.; Canals, B.; Coraux, J. Graphene as a Mechanically Active, Deformable Two-Dimensional Surfactant. *J. Phys. Chem. Lett.* **2018**, *9*, 2523−2531.
(18) Jin, L.; Fu, Q.; Mu, R.; Tan, D.; Bao, X. Pb Intercalation Underneath a Graphene Layer on Ru(0001) and its Effect on Graphene Oxidation. *Phys. Chem. Chem. Phys.* **2011**, *13*, 16655.
(19) Coraux, J.; N'Diaye, A. T.; Rougemaille, N.; Vo-Van, C.; Kimouche, A.; Yang, H.-X.; Chshiev, M.; Bendiab, N.; Fruchart, O.; Schmid, A. K. Air-Protected Epitaxial Graphene/Ferromagnet Hybrids Prepared by Chemical Vapor Deposition and Intercalation. *J. Phys. Chem. Lett.* **2012**, *3*, 2059−2063.
(20) Cui, Y.; Gao, J.; Jin, L.; Zhao, J.; Tan, D.; Fu, Q.; Bao, X. An Exchange Intercalation Mechanism for the Formation of a Two-Dimensional Si Structure Underneath Graphene. *Nano Res.* **2012**, *5*, 352−360.
(21) Vita, H.; Böttcher, S.; Leicht, P.; Horn, K.; Shick, A. B.; Máca, F. Electronic Structure and Magnetic Properties of Cobalt Intercalated in Graphene on Ir(111). *Phys. Rev. B* **2014**, *90*, 165432.
(22) Vlaic, S.; Kimouche, A.; Coraux, J.; Santos, B.; Locatelli, A.; Rougemaille, N. Cobalt Intercalation at the Graphene/Iridium(111) Interface: Influence of Rotational Domains, Wrinkles, and Atomic Steps. *Appl. Phys. Lett.* **2014**, *104*, 101602.
(23) Zhang, Y.; Zhang, H.; Cai, Y.; Song, J.; He, P. The Investigation of Cobalt Intercalation Underneath Epitaxial Graphene on 6H-SiC(0001). *Nanotechnology* **2017**, *28*, 075701.
(24) Rougemaille, N.; Vlaic, S.; Aballe, L.; Foerster, M.; Coraux, J. Confined Step-flow Growth of Cu Intercalated between Graphene and a Ru(0 0 0 1) Surface. *2D Mater.* **2019**, No. 035004.
(25) Drnec, J.; Vlaic, S.; Carlomagno, I.; Gonzalez, C. J.; Isern, H.; Carlà, F.; Fiala, R.; Rougemaille, N.; Coraux, J.; Felici, R. Surface Alloying upon Co Intercalation between Graphene and Ir(111). *Carbon* **2015**, *94*, 554−559.
(26) Cattelan, M.; Peng, G. W.; Cavaliere, E.; Artiglia, L.; Barinov, A.; Roling, L. T.; Favaro, M.; Píš, I.; Nappini, S.; Magnano, E.; Bondino, F.; Gavioli, L.; Agnoli, S.; Mavrikakis, M.; Granozzi, G. The Nature of the Fe-Graphene Interface at the Nanometer Level. *Nanoscale* **2015**, *7*, 2450−2460.
(27) Sutter, P.; Sadowski, J. T.; Sutter, E. Graphene on Pt(111): Growth and Substrate Interaction. *Phys. Rev. B* **2009**, *80*, 245411.
(28) Gao, M.; Pan, Y.; Huang, L.; Hu, H.; Zhang, L. Z.; Guo, H. M.; Du, S. X.; Gao, H.-J. Epitaxial Growth and Structural Property of Graphene on Pt(111). *Appl. Phys. Lett.* **2011**, *98*, No. 033101.
(29) N'Diaye, A. T.; Coraux, J.; Plasa, T. N.; Busse, C.; Michely, T. Structure of Epitaxial Graphene on Ir(111). *New J. Phys.* **2008**, *10*, No. 043033.
(30) Preobrajenski, A. B.; Ng, M. L.; Vinogradov, A. S.; Mårtensson, N. Controlling Graphene Corrugation on Lattice-mismatched Substrates. *Phys. Rev. B* **2008**, *78*, No. 073401.
(31) Pletikosić, I.; Kralj, M.; Pervan, P.; Brako, R.; Coraux, J.; N'Diaye, A. T.; Busse, C.; Michely, T. Dirac Cones and Minigaps for Graphene on Ir(111). *Phys. Rev. Lett.* **2009**, *102*, No. 056808.
(32) Dahal, A.; Addou, R.; Coy-Diaz, H.; Lallo, J.; Batzill, M. Charge Doping of Graphene in Metal/Graphene/Dielectric Sandwich Structures Evaluated by C-1s Core Level Photoemission Spectroscopy. *APL Mater.* **2013**, *1*, 042107.
(33) Maccariello, D.; Garnica, M.; Niño, M. A.; Navío, C.; Perna, P.; Barja, S.; Vázquez de Parga, A. L.; Miranda, R. Spatially Resolved, Site-dependent Charge Transfer and Induced Magnetic Moment in TCNQ Adsorbed on Graphene. *Chem. Mater.* **2014**, *26*, 2883−2890.
(34) Klimovskikh, I. I.; Otrokov, M. M.; Voroshnin, V. Y.; Sostina, D.; Petaccia, L.; Di Santo, G.; Thakur, S.; Chulkov, E. V.; Shikin, A. M. Spin-Orbit Coupling Induced Gap in Graphene on Pt(111) with Intercalated Pb Monolayer. *ACS Nano* **2017**, *11*, 368−374.
(35) Otrokov, M. M.; Klimovskikh, I. I.; Calleja, F.; Shikin, A. M.; Vilkov, O.; Rybkin, A. G.; Estyunin, D.; Muff, S.; Dil, J. H.; Vázquez de Parga, A. L.; Miranda, R.; Ochoa, H.; Guinea, F.; Cerdá, J. I.; Chulkov, E. V.; Arnau, A. Evidence of Large Spin-orbit Coupling Effects in Quasi-free-standing Graphene on Pb/Ir(111). *2D Mater.* **2018**, *5*, 035029.
(36) Dedkov, Y.; Voloshina, E. Graphene Growth and Properties on Metal Substrates. *J. Phys.: Condens. Matter* **2015**, *27*, 303002.
(37) Li, G.; Zhang, Y.-Y.; Guo, H.; Huang, L.; Lu, H.; Lin, X.; Wang, Y.-L.; Du, S.; Gao, H.-J. Epitaxial Growth and Physical Properties of 2D Materials beyond Graphene: from Monatomic Materials to Binary Compounds. *Chem. Soc. Rev.* **2018**, *47*, 6073.
(38) Vázquez de Parga, A. L.; Calleja, F.; Borca, B.; Passeggi, M. C. G., Jr.; Hinarejos, J. J.; Guinea, F.; Miranda, R. Periodically Rippled Graphene: Growth and Spatially Resolved Electronic Structure. *Phys. Rev. Lett.* **2008**, *100*, No. 056807.

https://dx.doi.org/10.1021/acsami.9b19159
ACS Appl. Mater. Interfaces 2020, 12, 4088−4096